Supplementary Information

Interactions at heterointerfaces influence actuation in wet cast 1T-MoS_2 and $V_2O_5 \cdot 0.5\ H_2O$ thin films

Jacob M. Baker,[1] Katelyn P. Murphy,[1] Michael L. Aubrey[1‡]

[1]*Department of Chemistry, University of Texas at Austin, Austin, TX 78712, USA.*

Table of Contents

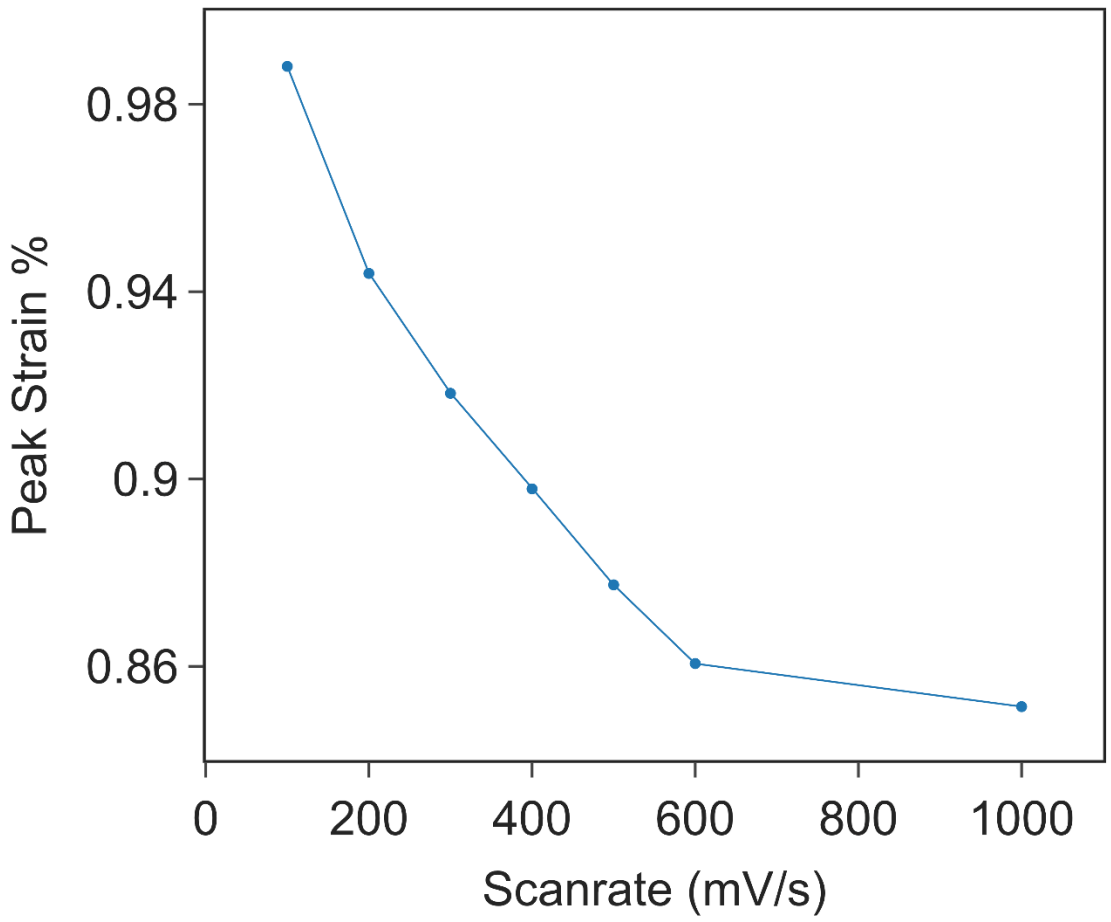

Figure S1. Peak Strain % values calculated during actuation of a 1T-MoS_2 | Au | Kapton electrode at various potential scan rates. CV was performed in 0.5 M Na_2SO_4 aqueous electrolyte with platinum wire counter and Ag/AgCl reference electrodes over a potential window of -0.3 to 0.3 V.

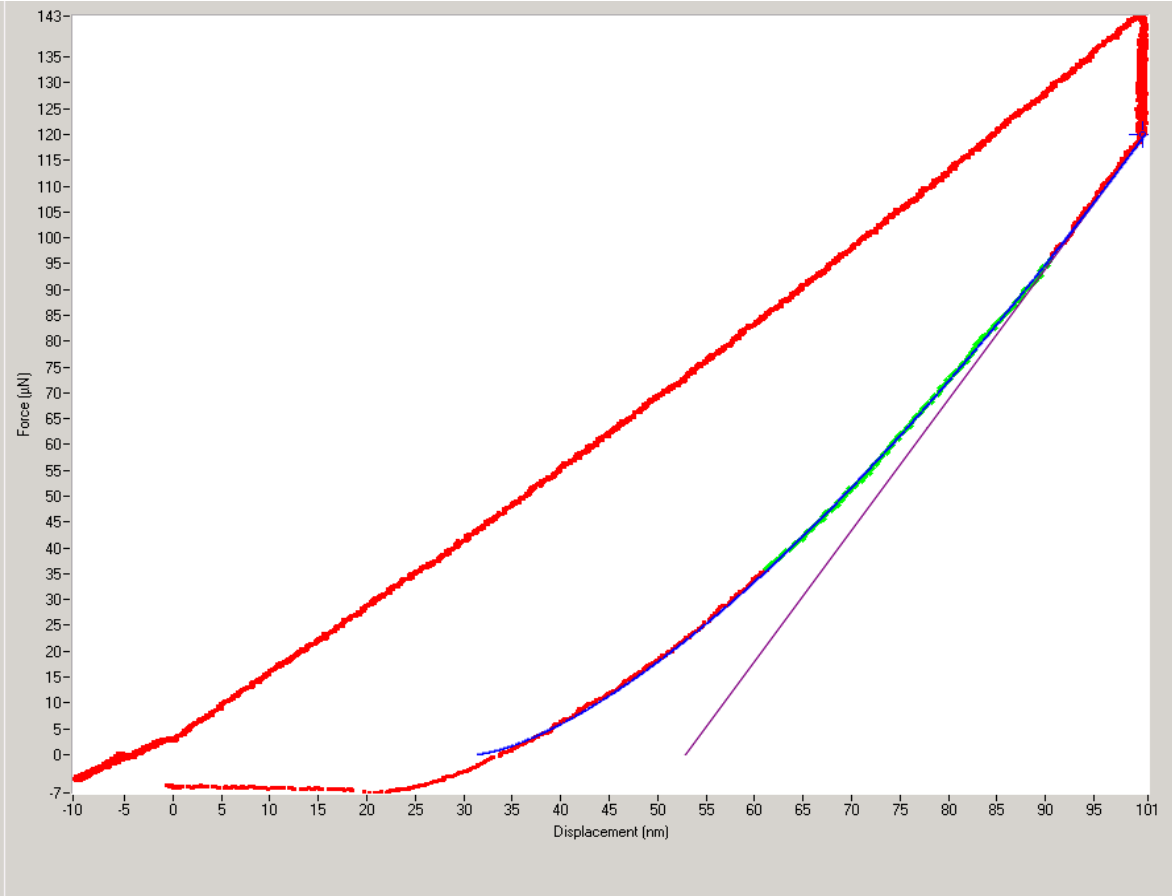

Figure S2. Nanoindentation measurement of deposited 1T-MoS_2. Indent depth was kept below ~ 10% of the active layer thickness to avoid influence from the substrate. Based on the displacement response to the applied force, an out of plane Young's modulus of 5.01 GPa and was converted to the in-plane Young's modulus using the Poisson ratio of 1T-MoS_2 (0.3) and was found to be 1.50 GPa.[54]

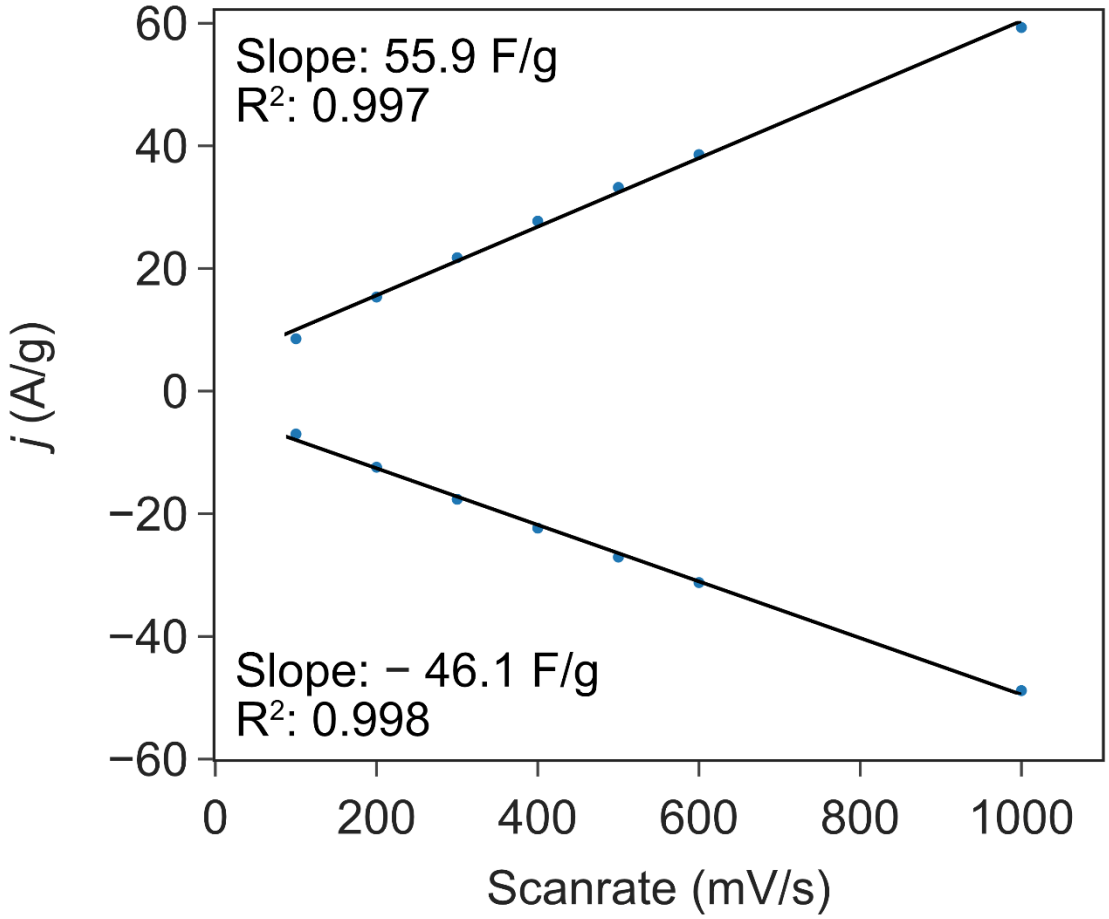

Figure S3. Charging current for a 1T-MoS_2 | Au | Kapton electrode plotted vs scan rate. The slope represents the specific capacitance in F/g for the positive and negative charging current centered around 0 V vs Ag/AgCl respectively. CV was performed in 0.5 M Na_2SO_4 aqueous electrolyte with platinum wire counter and Ag/AgCl reference electrodes over a potential window of -0.3 to 0.3 V.

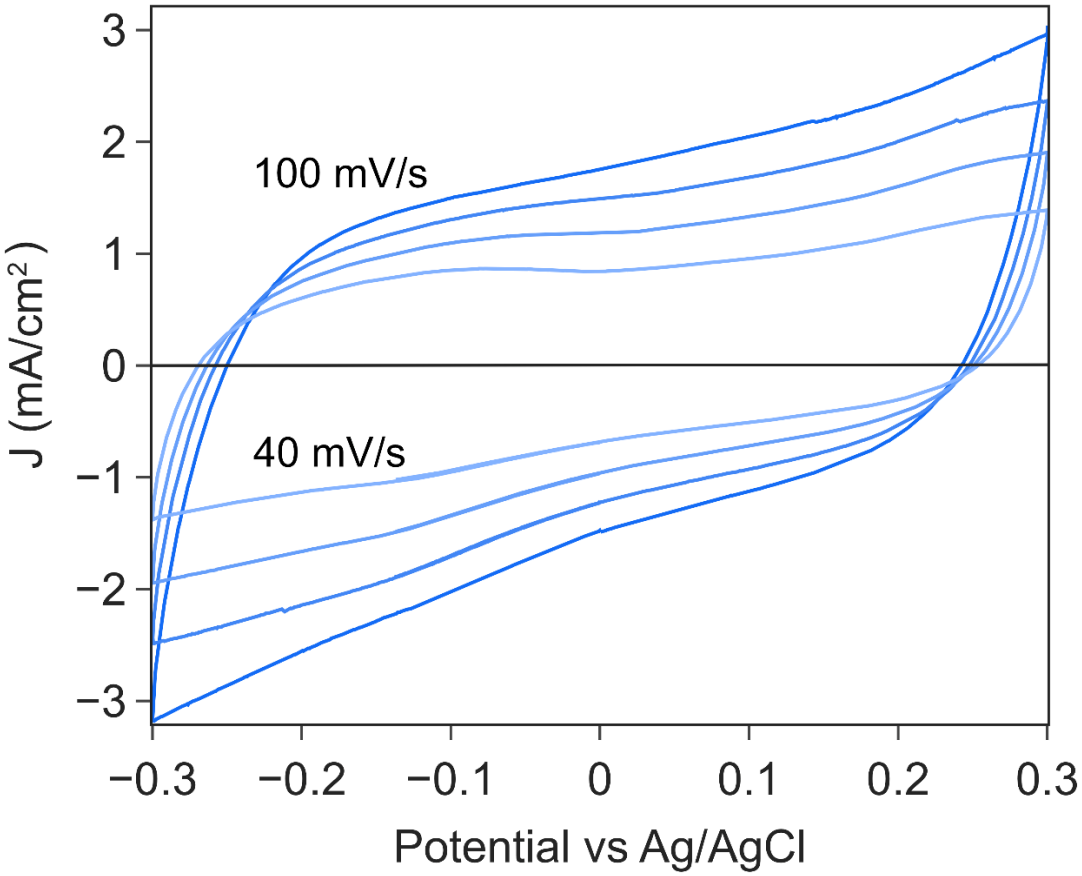

Figure S4. CV of 1T-MoS_2 | Ni | Kapton taken in 0.5 M Na_2SO_4 aqueous electrolyte with platinum wire counter and Ag/AgCl reference electrodes at scan rates of 40, 60, 80, and 100 mV/s.

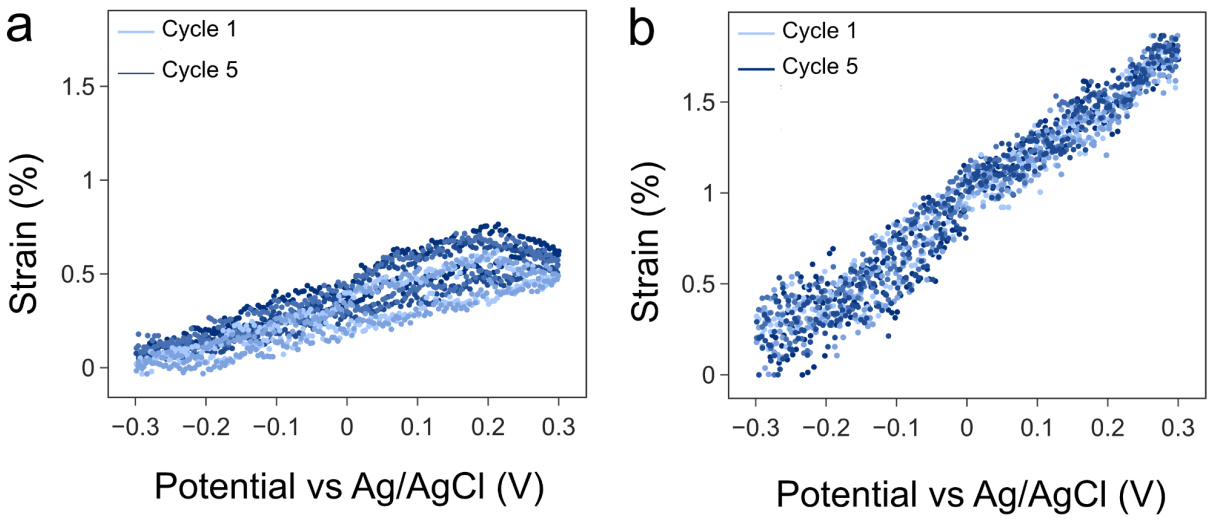

Figure S5. a) Strain % versus potential of 1T-MoS_2 | Ni | Kapton electrode for five cycles. Rearrangement or creep of active layer results in shift in strain % on the Ni substrate but the shape remains consistent. b) Strain % versus potential of 1T-MoS_2 | Au | Kapton electrode for five cycles.

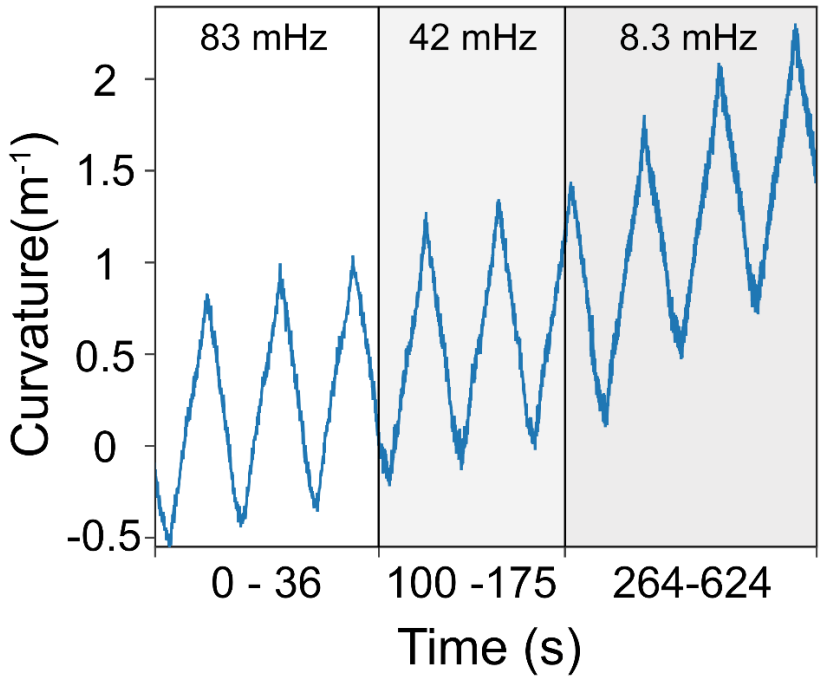

Figure S6. Scan rate dependence of 1T-MoS_2 | Ni | Kapton electrode at scan rates of 100, 50, and 10 mV/s. CV was performed in 0.5 M Na_2SO_4 aqueous electrolyte with platinum wire counter and Ag/AgCl reference over a potential window of -0.3 to 0.3 V. Maximum change in curvature is consistent within error between all three scan rates.

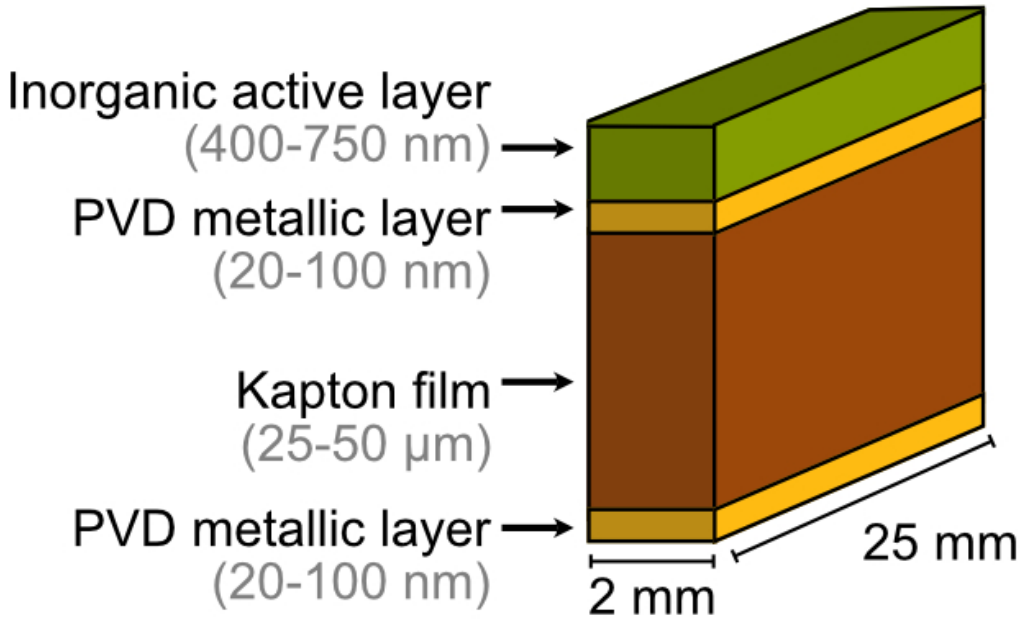

Figure S7. Schematic of $V_2O_5 \cdot 0.5\ H_2O$ | Au | Kapton electrode with double sided metal coatings to prevent issues with swelling of Kapton in organic electrolytes. Electrodes were fabricated by methods described in main text.

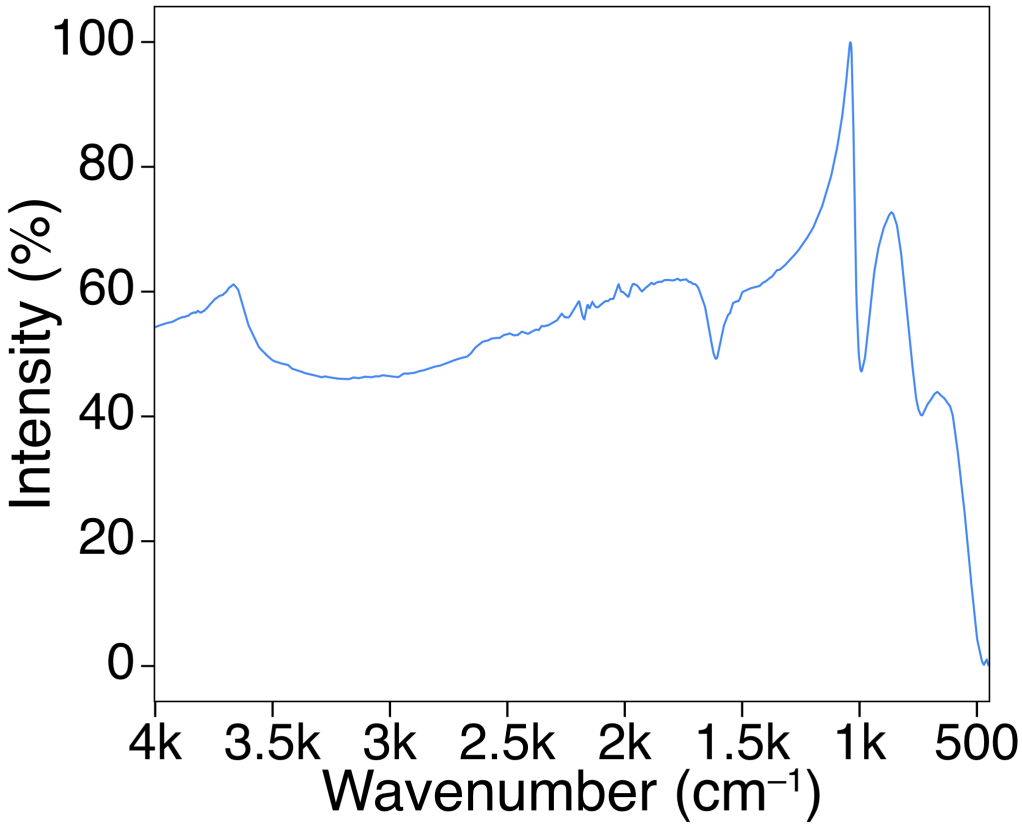

Figure S8. Infrared spectrum of $V_2O_5 \cdot 0.5\ H_2O$ bulk material. Broad hump at 3000 cm^{-1} and peak at 1600 cm^{-1} are due to stretching and bending vibrations of OH groups, peak at 992 cm^{-1} is vanadyl stretching vibration (V=O), and peaks at 738 and 472 cm^{-1} are due to bridging V-O-V and V-O stretching vibrations respectively.

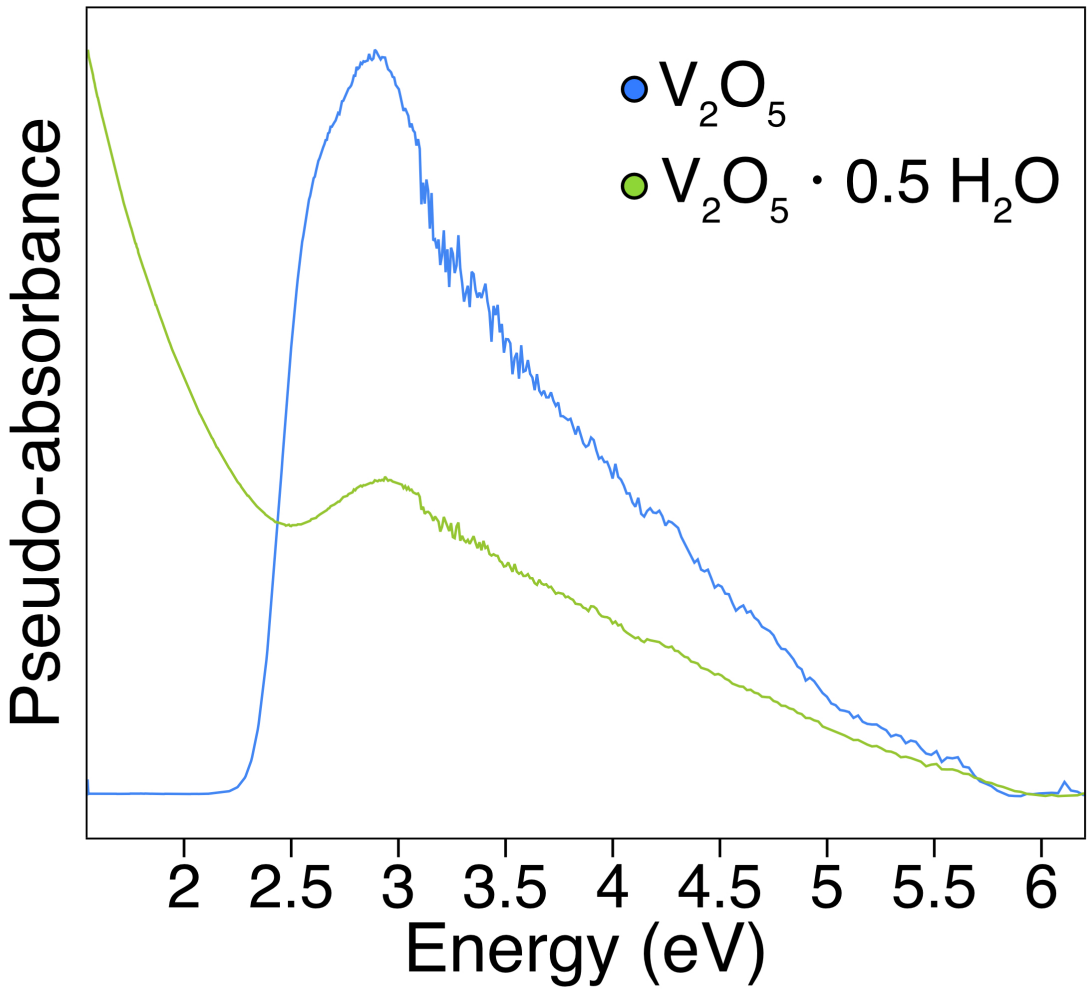

Figure S9. Ultraviolet-visible absorption spectrum (UV-vis) of synthesized $V_2O_5 \cdot 0.5\ H_2O$ bulk material and V_2O_5 starting material diffuse reflectance data was converted to pseudo absorbance spectra using Kubelka-Munk transformation. V_2O_5 is initially a bright orange color but during synthesis of hydrate becomes dark green/black color as reflected by increased absorbance in low energy region.

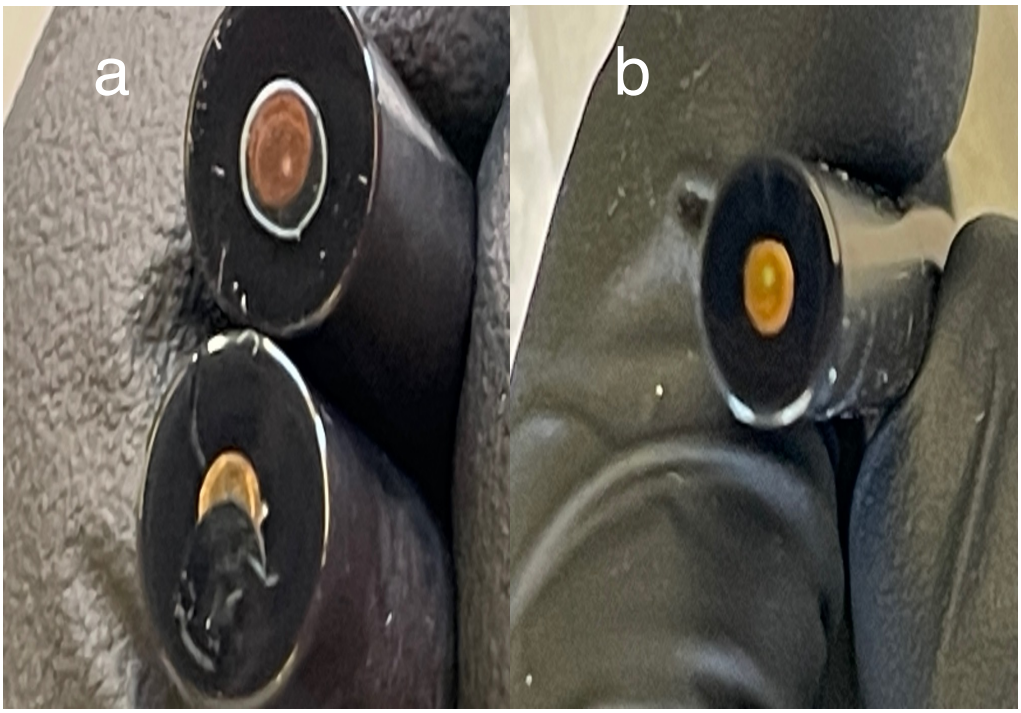

Figure S10. Measurements taken in 0.5 M $NaClO_4$ propylene carbonate electrolyte with platinum wire counter and Ag/Ag^+ reference electrodes at scan rate of 0.1 mV/s. (a) Images of $V_2O_5 \cdot 0.5\ H_2O$ | Au disc electrodes, top electrode is as prepared by drop casting $V_2O_5 \cdot 0.5\ H_2O$ onto Au disc electrodes and drying. After applying at 0 V vs Ag/Ag^+ for 30 minutes, the $V_2O_5 \cdot 0.5\ H_2O$ film became a dark black seen in the bottom electrode. (b) Image of $V_2O_5 \cdot 0.5\ H_2O$ | Au disc electrode after holding at 1.3 V vs Ag/Ag^+ for 30 minutes after having cycled the electrode within a potential window of 0 V to 1.3 V 10 times. Return of orange color of $V_2O_5 \cdot 0.5\ H_2O$ film is due to oxidation of V^{4+} to V^{5+} showing reversibility of electrochemical reaction.

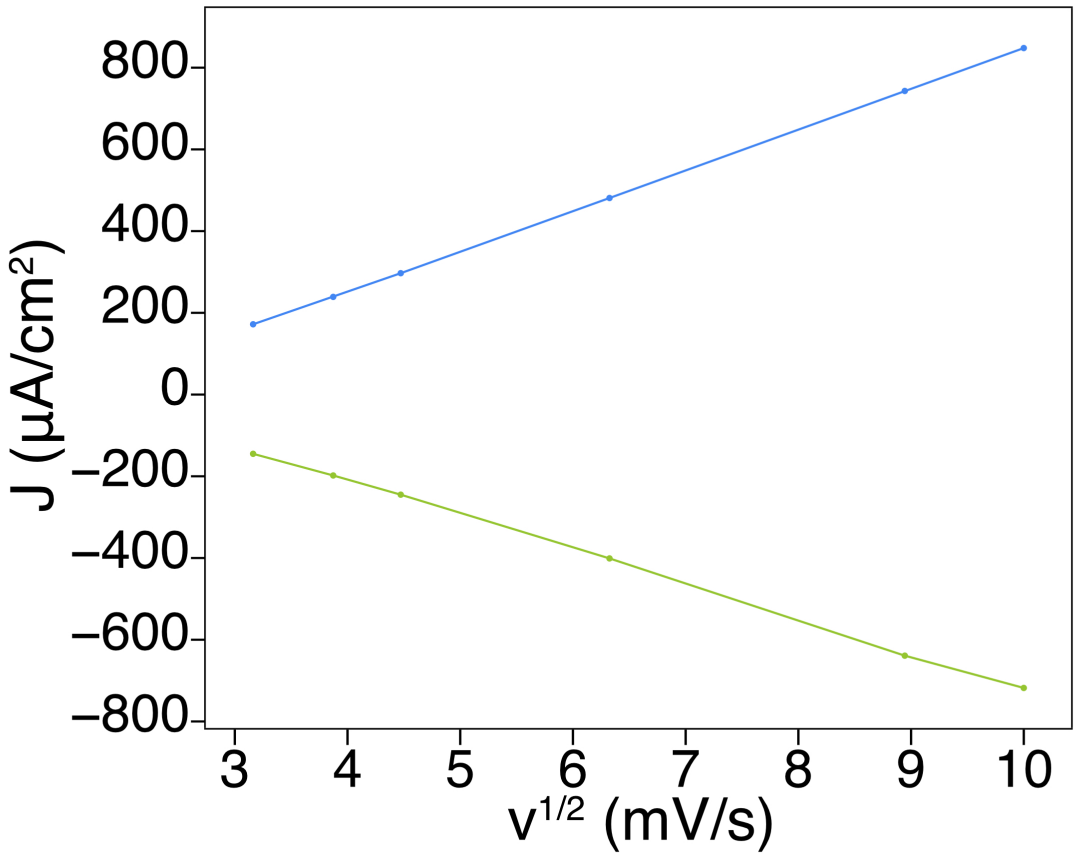

Figure S11. Plots of peak current density J (μA/cm^2) versus square root of the scan rate in a $V_2O_5 \cdot 0.5\ H_2O$ | Au | Kapton electrode taken in 0.5 M $NaClO_4$ propylene carbonate electrolyte with platinum wire counter and Ag/$AgNO_3$ reference electrodes at scan rates of 10, 15, 20, 40, 80, and 100 mV/s. Linearity of the plot indicates a reversible diffusion limited process.

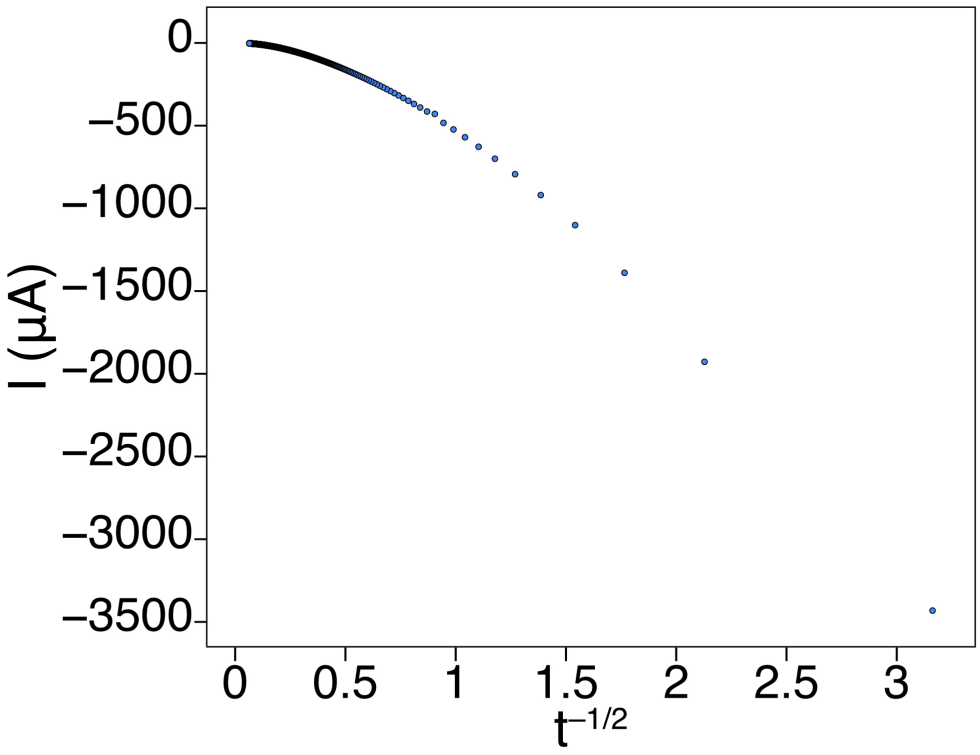

Figure S12. Plot of current (μA) versus inverse square root of time ($s^{-1/2}$) in a $V_2O_5 \cdot 0.5\ H_2O$ | Au | Kapton electrode taken in 0.5 M $NaClO_4$ propylene carbonate electrolyte with platinum wire counter and $Ag/AgNO_3$ reference electrodes at potential limits of -0.8 V and 1.0 V and held for 4 minutes. Linearity of the plot indicates a reversible Cottrell diffusion limited process.

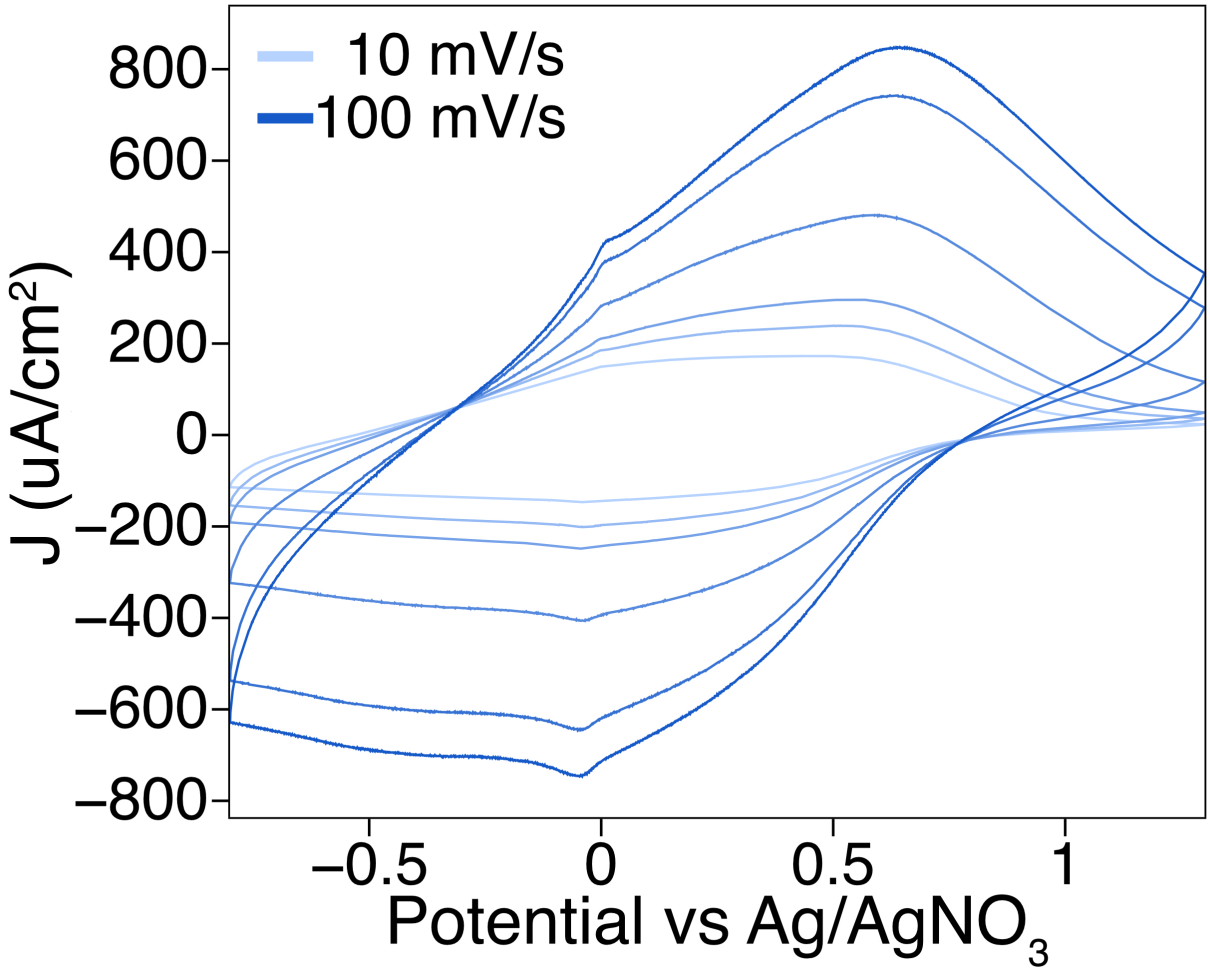

Figure S13. CV of $V_2O_5 \cdot 0.5\ H_2O$ | Au | Kapton taken in 0.5 M $NaClO_4$ propylene carbonate electrolyte with platinum wire counter and $Ag/AgNO_3$ reference electrodes at scan rates of 10, 15, 20, 40, 80, and 100 mV/s.

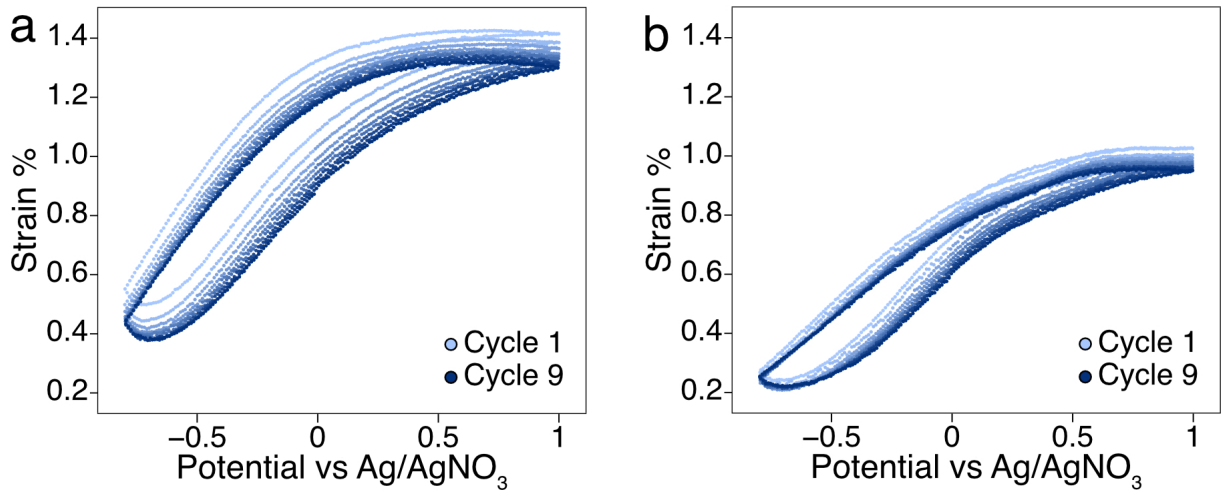

Figure S14. a) Strain % versus potential of $V_2O_5 \cdot 0.5\ H_2O$ | Ni | Kapton electrode for nine cycles. During initial cycles rearrangement or creep of active layer results in shift in strain % achieved but stabilizes with further cycling. b) Strain % versus potential of $V_2O_5 \cdot 0.5\ H_2O$ | Au | Kapton electrode for nine cycles.

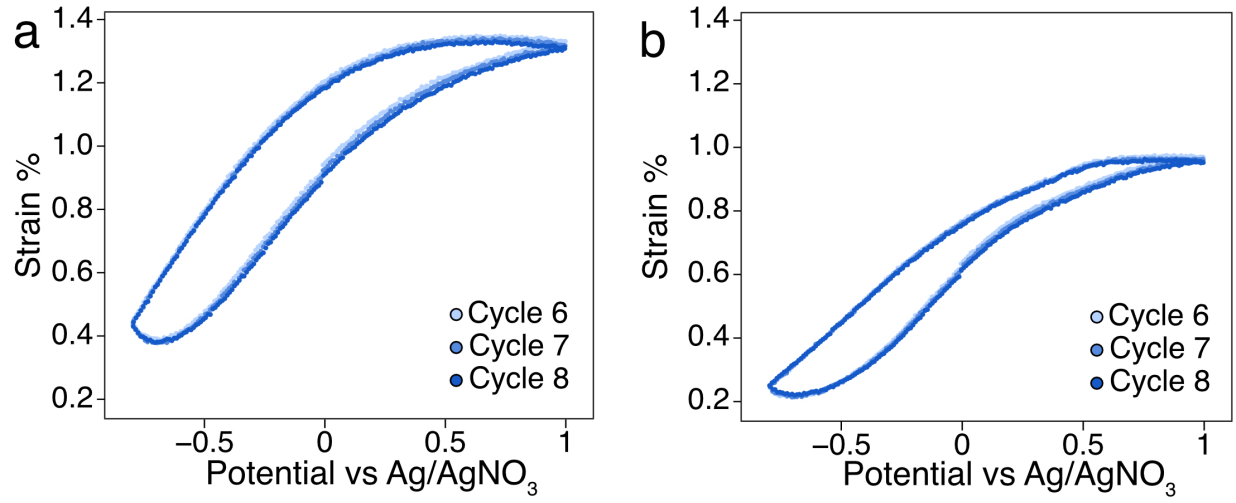

Figure S15. a) Strain % versus potential of $V_2O_5 \cdot 0.5\ H_2O$ | Ni | Kapton electrode for three cycles after creep/rearrangement of active layer. b) Strain % versus potential of $V_2O_5 \cdot 0.5\ H_2O$ | Au | Kapton electrode for three cycles after creep/rearrangement of active layer.

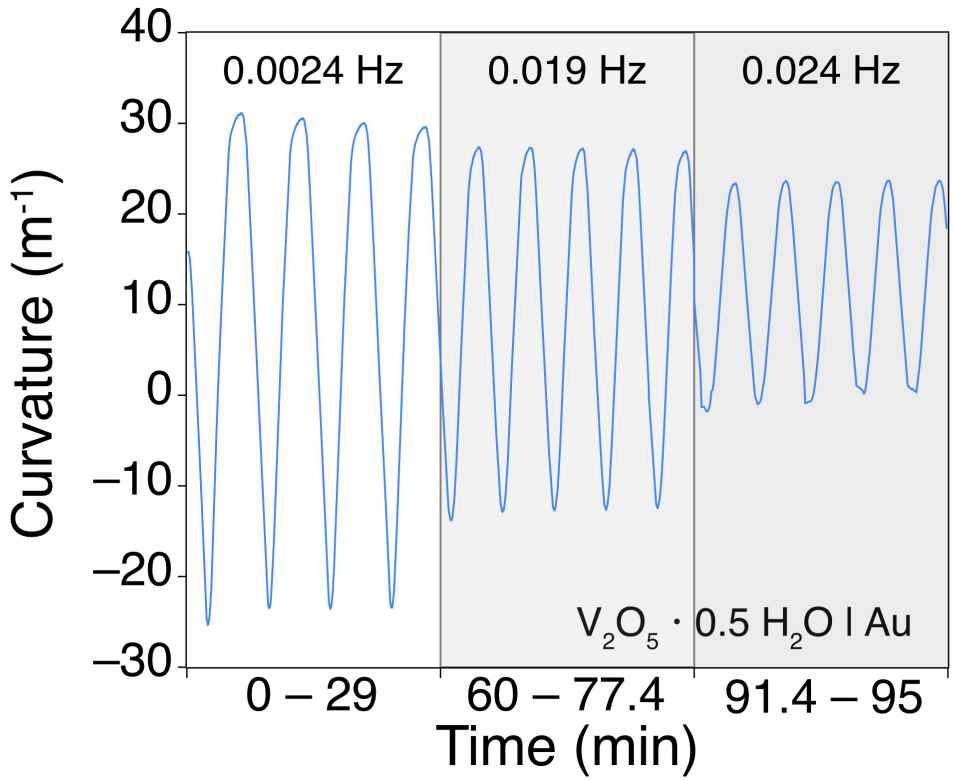

Figure S16. Scan rate dependence of $V_2O_5 \cdot 0.5\ H_2O$ | Au | Kapton electrode at scan rates of 10, 40, and 100 mV/s taken in 0.5 M $NaClO_4$ propylene carbonate electrolyte with platinum wire counter and $Ag/AgNO_3$ reference electrodes.

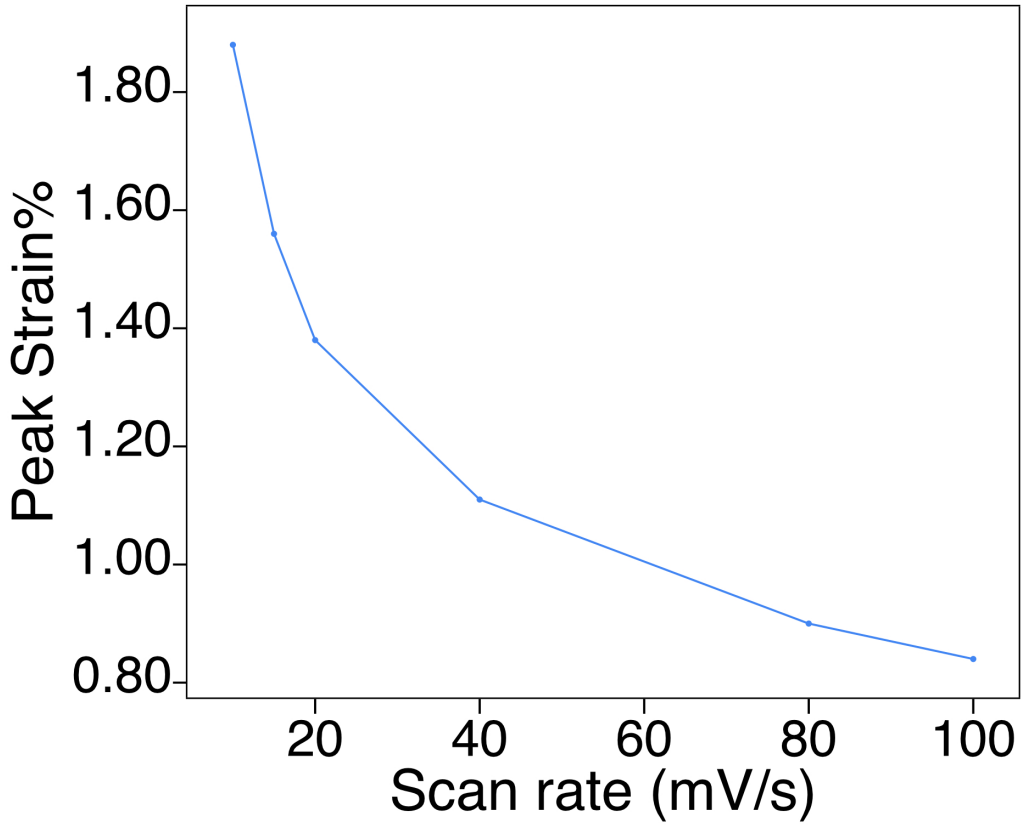

Figure S17. Peak Strain% values calculated during actuation at various potential scan rates in a $V_2O_5 \cdot 0.5\ H_2O$ | Au | Kapton actuator taken in 0.5 M $NaClO_4$ propylene carbonate electrolyte with platinum wire counter and $Ag/AgNO_3$ reference electrodes at scan rates of 10, 15, 20, 40, 80, and 100 mV/s.

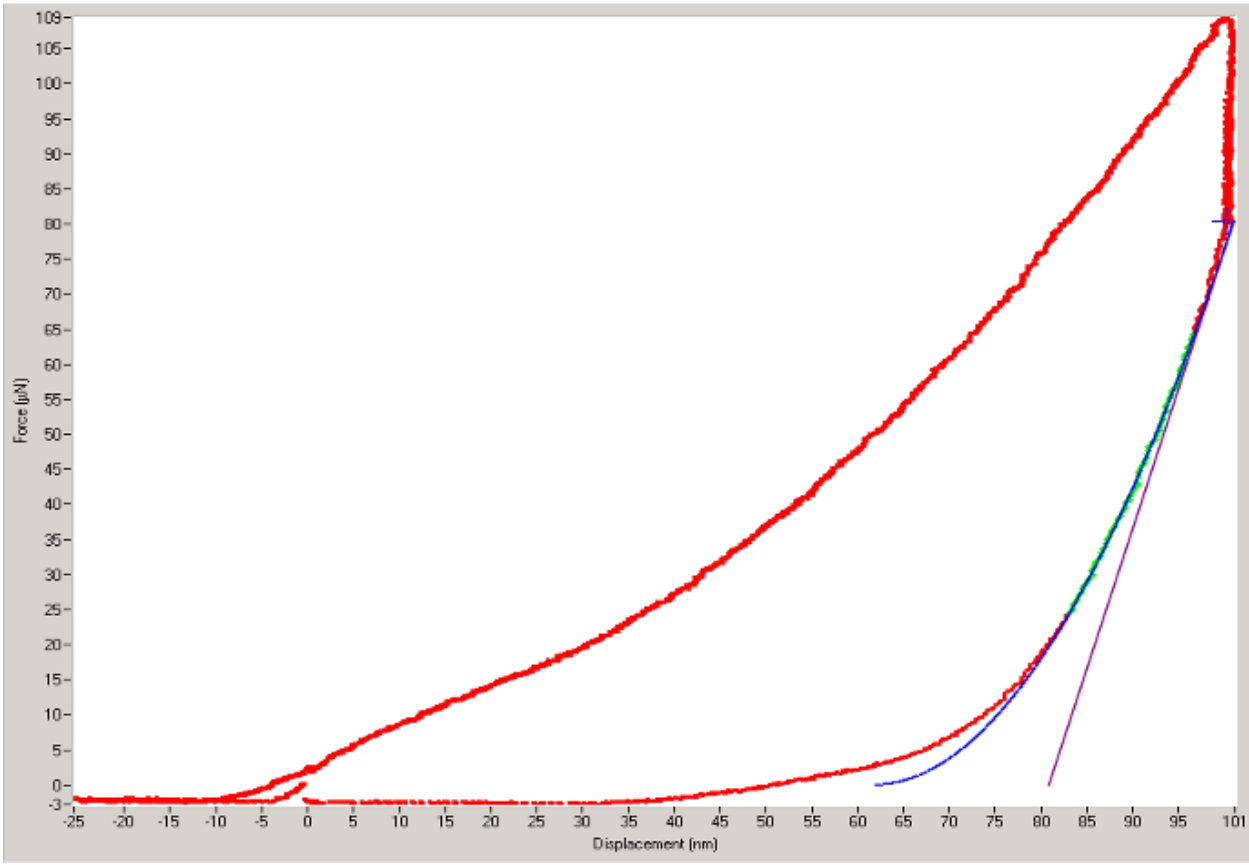

Figure S18. Nanoindentation of deposited $V_2O_5 \cdot 0.5\ H_2O$. Indent depth was kept below ~ 10% of the active layer thickness to avoid influence from the substrate. Based on the displacement response to the applied force an out of plane Young's modulus of 6.21 GPa and was converted to the in-plane Young's modulus using Acerce's method and the Poisson ratio of V_2O_5 (0.24) which was found as 1.46 GPa.[67]

Table S1. Summary of actuator changes in curvature observed and strains, stress, and moduli calculated based on the known crystallographic strain for $Na_xV_2O_5 \cdot 0.5\ H_2O$ | M | Kapton electrodes where M is metal layer identity.

Measurement	Curvature	Strain %	Stress (Mpa)	Modulus	Samples
Au-CV	18(3)	1.84(0.10)	16(2)	0.9(1)	6
Au-CA	20(3)	2.15(0.10)	18(3)	0.8(1)	6
Ni-CV	16(1)	2.24(0.12)	11.7(6)	0.56(2)	7
Ni-CA	22(2)	2.47(0.10)	17(1)	0.68(3)	7

Table S2. Stresses due to actuation calculated for $V_2O_5 \cdot 0.5\ H_2O$ | M | Kapton electrodes using the Stoney model where M is the metal layer identity.

Electrode-measurement	Stoney Stress (MPa)
$V_2O_5 \cdot 0.5\ H_2O$ | Au | Kapton-CV	15(2)
$V_2O_5 \cdot 0.5\ H_2O$ | Au | Kapton-CA	16(2)
$V_2O_5 \cdot 0.5\ H_2O$ | Ni | Kapton-CV	10.8(5)
$V_2O_5 \cdot 0.5\ H_2O$ | Ni | Kapton-CA	16(1)

Table S3. Stresses due to actuation calculated for 1T-MoS_2 | M | Kapton electrodes using the Stoney model.

Electrode-measurement	Stoney Stress (MPa)
1T-MoS_2 | Au | Kapton-CV	17(2)
1T-MoS_2 | Au | Kapton-CA	15.3(0.8)
1T-MoS_2 | Ni | Kapton-CV	5.3(0.5)
1T-MoS_2 | Ni | Kapton-CA	4.5(0.4)

Table S4. Summary of reported V_2O_5 based actuators Strain %, active layer modulus, generated Stress, and fabrication method where NW is nanowires, SWCNT is single walled carbon nanotubes, and CNTF is carbon nanotube fiber.

Actuator	Strain %	Modulus (Gpa)	Stress (Mpa)	Fabrication	Reference
V_2O_5 NWs	0.21	4.8	5.9	Entangled nanowires in cellulose filter by vacuum filtration	12
V_2O_5 NW/SWCNT	0.18	NR	1.54E-03	Entangled V_2O_5 and SWCNT by vacuum filtration	78
V_2O_5 NW/CNTF	NR	15.4	NR	Wet twisting V2O5 NW and CNTF	24
$V_2O_5 \cdot 0.5$ H_2O | Au	1.24(0.20)	1.46	18(3)	Wet cast thin film	This work
$V_2O_5 \cdot 0.5$ H_2O | Ni	1.17(0.08)	1.46	17(1)	Wet cast thin film	This work

Table S5. Summary of reported MoS_2 based actuators Strain %, active layer modulus, generated Stress, and fabrication method where pMoS_2-nSNrGO is oxide-doped p-type MoS_2 and sulfur-nitrogen-doped n-type graphene, PDMS is polydimethylsiloxane, and PVDF is polyvinylidene difluoride.

Actuator	Strain %	Modulus (Gpa)	Stress (Mpa)	Fabrication	Reference
Polymer nanocomposite	2-5	NR	0.03	2 wt. % ultrafine 2H-MoS_2 powder in PDMS	79
MoS_2-carbon nanotube-polymer	0.76	0.571-0.771	NR	Bulk 2H-MoS_2 powder mixed with PVDF and carbon nanotubes and dried into a gel	80
pMoS_2-nSNrGO nanohybrid	1.2	0.106	NR	Hydrothermal synthesis of "flower-like" nanohybrid, MoS_2 nanoparticles atop graphene petals	81
1T-MoS_2 nanosheets	0.6	2-4	17	Restacked nanosheets from liquid suspension by vacuum filtration over nitrocellulose membrane and subsequent transfer to Au-Kapton substrate	82
1T-MoS_2 film on PVDF	NR	0.0986	NR	Restacked nanosheets from liquid suspension by vacuum filtration over PVDF membrane	83
MoS_2 | Au	1.29(0.13)	1.50	15(1)	Wet cast thin film	This work
MoS2 | Ni	0.57(0.05)	1.50	7.8(0.6)	Wet cast thin film	This work

References:

78. Y. Ling, H. Fan, K. Wang, Z. Lu, L. Wang, C. Hou, Q. Zhang, Y. Li, K. Li and H. Wang, *Small*, 2022, 18, 2107778.
79. X. Fan, F. Khosravi, V. Rahneshin, M. Shanmugam, M. Loeian, J. Jasinski, R. W. Cohn, E. Terentjev, B. Panchapakesan, *Nanotechnology,* 2015, 26, 261001.
80. D. Gendron, G. Bubak, L. Ceseracciu, F. Ricciardella, A. Ansaldo, D. Ricci, *Sens. Actuators. B. Chem.*, 2016, 230, 673-683
81. M. T. Manzoor, V. H. Nguyen, S. Umrao, J. -H. Kim, R. Tabassian, J. -E. Kim, I. -K. Oh, *Adv. Funct. Mater.*, 2019, 29, 1905454.
82. M. Acerce, E. K. Akdogan and M. Chhowalla, *Nature*, 2017, 549, 370–373.
83. H. Li, H. Yang, C. Xu, X. Cheng, J. Yan, K. Cen, Z. Bao, K. Ostrikov, *J. Thermal Sci. Eng. Appl.*, 2022, 14, 125001.